Arch Appl Mech (2012) 82:709–722
DOI 10.1007/s00419-011-0585-1

ORIGINAL

Qinkai Han · Fulei Chu

Dynamic instability and steady-state response of an elliptical cracked shaft

Received: 30 December 2010 / Accepted: 30 August 2011 / Published online: 20 September 2011

Abstract An elliptical front crack has been found to be more accurate and realistic for modeling the transverse surface crack in rotating machinery compared with the widely used straight front crack. When the shaft rotates, the elliptical crack opens and closes alternatively, due to gravity, and thus, a "breathing effect" occurs. This variance in shaft stiffness is time-periodic, and hence, a parametrically excited system is expected. Therefore, the dynamic instability and steady-state response of a rotating shaft containing an elliptical front crack are studied in the paper. The local flexibility due to the crack is derived, and the governing equations of the crack shaft system are established using the assumed modes method. Utilizing the Bolotin's method and harmonic balance method, the boundaries of two typical instability regions and maximum response amplitude of the cracked shaft could be computed numerically. The elliptical crack parameters (depth, shape factor and position) and damping are, respectively, considered and discussed for their effects on the dynamic behavior of the elliptical cracked shaft. Some research results might be helpful for the crack detection in rotating machinery.

Keywords Rotating shaft · Elliptical surface crack · Breathing effect · Dynamic instability · Steady-state forced response

1 Introduction

Shafts are among components subjected to, perhaps, the most arduous working conditions in high-performance rotating equipment used in process and utility plants. Due to manufacturing flaws or cyclic loading, cracks frequently appear in rotating machinery. The growth of cracks in the rotating components can cause severe accidents if undetected. It is well known that a surface crack introduces local flexibilities and then alters the vibrational behavior of the shaft. Thus, the dynamic behavior of a rotating shaft containing a transverse surface crack, which is useful for the crack detection in rotating machinery, has been investigated since the 1970s. Early research progress could be found in [1–3]. Recently, more detailed reviews of the crack modeling and diagnosis were given by Papadopoulos [4] and Bachschmid [5], respectively.

In many of those works, a straight edge is usually considered to idealize the surface crack front [6–8]. However, it is shown from the experimental observations [9,10] that the actual surface crack front in shaft under cyclical bending or axial load tends to be a curve rather than a straight line. The problem is largely solved using an elliptical arc to model the surface crack front [11,12]. As the literature shows, extensive efforts

Q. Han (✉) · F. Chu
Department of Precision Instruments and Mechanology, Tsinghua University, Beijing 100084, China
E-mail: hanqinkai@hotmail.com
Tel.: +861062788308
Fax: +861062788308

F. Chu
E-mail: chufl@mail.tsinghua.edu.cn

have been devoted to calculating the stress intensity factors (SIF) and then analyzing the fatigue growth of an elliptical surface crack in a shaft or round bar [13–17], while the dynamic behavior of an elliptical cracked shaft has not gained sufficient attentions. In the pioneering work by Rubio [18,19], flexibility expressions for cracked shafts having elliptical front cracks under bending or axial tension load were obtained, based on the strain energy release rate (SERR) approach and the polynomial fitting of SIF, taking into account the size and shape of the elliptical cracks. When the shaft rotates, the elliptical crack opens and closes alternatively, due to gravity, and thus, a "breathing effect" occurs. This variance in shaft stiffness is time-periodic, and hence, a parametrically excited system is expected. The parametric excitation from the time-varying shaft stiffness causes instability and severe vibration under certain operating conditions.

Therefore, the dynamic instability and steady-state response of an elliptical cracked shaft under both parametric and self-weight excitations are studied in the paper. First, local flexibility coefficients in two transverse directions by Rubio [18] are adopted, and the time-periodic local compliance due to shaft rotating is fitted through a similar approach in Ref. [6]. Then, the governing equations of a rotating elliptical cracked shaft are obtained in virtue of the assumed modes method. The Bolotin's method and harmonic balance method are, respectively, introduced for determining the unstable boundaries and steady-state forced responses. Based upon these, a practical used heavy rotating shaft is taken as a numerical example. Boundaries of two typical instability regions and variations of maximum vibrational amplitude with shaft rotating speed are solved. The effects of crack parameters (crack depth, shape factor and position) and damping on the dynamic behavior of cracked rotating shaft are discussed, respectively. Finally, some useful conclusions are given.

2 Elliptical crack modeling

Rubio [18,19] employed the SIF solutions for the elliptical front crack and formulated flexible coefficients of an elliptical cracked shaft submitted to bending moments M and axial loads T using the SERR approach. In the derivation, the axial flexibility was coupled with that of the bending. It was shown, however, that if the bending moment dominated in the shaft, the coupling terms might be neglected. In current research, the bending moment M is of the most significance, and hence, the corresponding flexibility is only considered.

The cross-section of a circular shaft with an elliptical transverse crack is shown in Fig. 1. The radius of the circular cross-section, major and minor axes of the crack ellipse are, respectively, denoted as R, b and a. The points A and B are the intersection points between the crack ellipse and circular. Point C is an arbitrary point on the elliptical arc s. The projection lengths of points A and C upon the axis $O\xi$ are expressed as h and ξ_1. The characteristic parameters of an elliptical crack are as follows: crack depth $\alpha = a/R$, shape factor $\beta = a/b$ and relative position in the front of the crack $\gamma = \xi_1/h$.

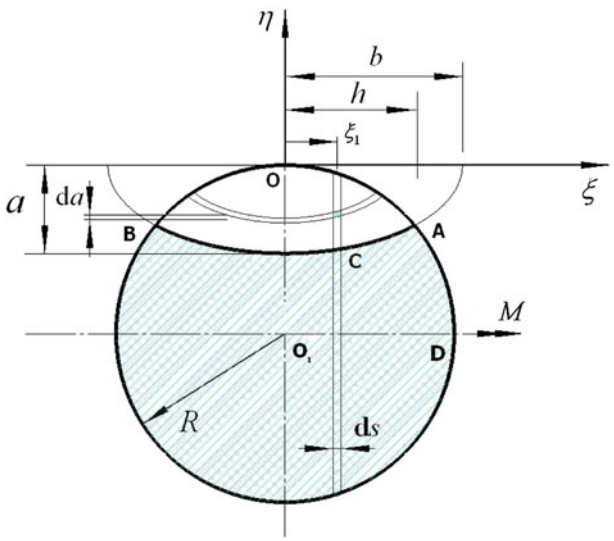

Fig. 1 Cross-section of a circular shaft with an elliptical transverse crack

According to the Castigliano theorem, the local flexibility of the crack due to bending moment in the $O\xi$ direction is obtained as

$$c_\xi = \frac{\partial^2}{\partial M^2}\left(\int_{A_c} \Im \mathrm{d}A_c\right) \tag{1}$$

where $\Im$ is the energy release rate due to the crack growth (or called strain energy density function), and A_c is the crack surface area. For the surface crack under bending moment, the SIF with mode I, K_I, is the only non-zero one. Considering the formulation of linear fracture mechanics, the relationship between the $\Im$ and K_I in plane strain conditions is

$$\Im = \frac{1-\nu^2}{E} K_I^2 \tag{2}$$

in which E is the Young's modulus and ν is Poisson's ratio. With the geometrical dimensions defined in Fig. 1, the K_I of the elliptical surface crack for the M in the $O\xi$ direction can be expressed in the following form

$$K_I = F_{I,1}(\alpha, \beta, \gamma)\sigma_M \sqrt{\pi a} \tag{3}$$

where σ_M is the maximum bending stress in the circular cross-section ($\sigma_M = 4M/(\pi R^3)$), and $F_{I,1}(\alpha, \beta, \gamma)$ is the geometry correction factor. Experimental backtracking technique and finite element analysis have been employed by Shin [17] to evaluate the stress intensities along the front of an elliptical surface crack. A closed-form expression of $F_{I,1}(\alpha, \beta, \gamma)$ using a multi-parameter fitting technique could be found in [17]. Substituting Eq. (3) into (2), and then into Eq. (1), one can have

$$c_\xi = \frac{1-\nu^2}{E}\frac{32}{\pi R^6}\left(\int_{A_c} F_{I,1}^2(\alpha, \beta, \gamma) a \mathrm{d}A_c\right) \tag{4}$$

in which $\mathrm{d}A_c = \mathrm{d}s\mathrm{d}a$. The elliptical arc differential $\mathrm{d}s$ takes the form

$$\mathrm{d}s = a\sqrt{\frac{1}{\beta^2}\sin^2\phi + \cos^2\phi}\mathrm{d}\phi \tag{5}$$

Substituting Eq. (5) into (4) and considering the symmetrical distribution of K_I about the $O\eta$ axis ($\phi = \pi/2$), one can obtain

$$c_\xi = \frac{1-\nu^2}{E}\frac{64}{\pi R^3}\int_0^{\alpha_f}\int_{\phi_1}^{\pi/2} F_{I,1}^2(\alpha, \beta, \gamma)\alpha^2\sqrt{\frac{1}{\beta^2}\sin^2\phi + \cos^2\phi}\mathrm{d}\phi\mathrm{d}\alpha \tag{6}$$

where α_f is the nominal crack depth, ϕ_1 is the lower limit and $\cos\phi_1 = \bar{h}$. According to the geometry dimensions in Fig. 1, one can have

$$\bar{h} = h/b = \beta\sqrt{\frac{2\sqrt{\beta^4 + (1-\beta^2)\alpha^2} - (1-\beta^2)\alpha^2 - 2\beta^2}{(1-\beta^2)^2\alpha^2}} \quad (\beta \neq 1) \tag{7}$$

$$\bar{h} = h/b = \sqrt{1 - \alpha^2/4} \quad (\beta = 1) \tag{8}$$

In computation, the relative position γ should be substituted by $\frac{1}{\bar{h}}\cos\phi$. When the bending moment M is in the $O\eta$ direction, the SIF along the crack front could be expressed similarly as

$$K_I = F_{I,2}(\alpha, \beta, \gamma)\sigma_M \sqrt{\pi a} \tag{9}$$

For the elliptical cracked shaft under bending moment in the $O\eta$ direction, all the numerical results about the $F_{I,2}(\alpha, \beta, \gamma)$ deduced through finite element analysis were displayed in Ref. [13], where α ranges from 0.2 to 1.2, and β varies from 0 to 1.2. Here, a closed-form expression of $F_{I,2}(\alpha, \beta, \gamma)$ is obtained using a

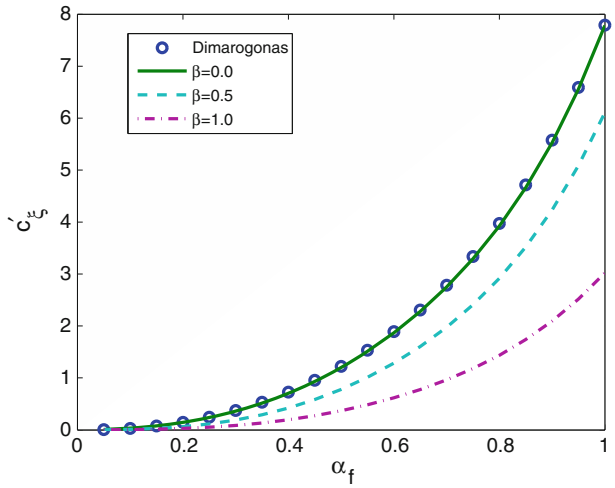

Fig. 2 Variations of c'_ξ with α_f in the range of 0–1 for various β

multi-parameter fitting technique. Similar to the computation of c_ξ, the flexibility coefficient c_η in the $O\eta$ direction is written as

$$c_\eta = \frac{1-\nu^2}{E}\frac{32}{\pi R^3}\int_0^{\alpha_f}\int_{\phi_1}^{\pi/2} F_{I,2}^2(\alpha,\beta,\gamma)\alpha^2\sqrt{\frac{1}{\beta^2}\sin^2\phi+\cos^2\phi}\,\mathrm{d}\phi\mathrm{d}\alpha \tag{10}$$

Something should be mentioned is that only half of the crack surface is in tension stress condition for the bending moment in the $O\eta$ direction. Thus, $A_c/2$ is adopted in analysis. In order to facilitate the following analysis, dimensionless forms of flexibility coefficients are defined

$$c'_\xi = \frac{ER^3}{1-\nu^2}c_\xi, \quad c'_\eta = \frac{ER^3}{1-\nu^2}c_\eta \tag{11}$$

Utilizing the double numerical integration technique, the flexibility coefficients c'_ξ, c'_η are solved with given crack depth α_f and shape factor β. Figure 2 gives the variations of c'_ξ with α_f in the range of 0 to 1 for various shape factors ($\beta = 0, 0.5, 1.0$). Obviously, $\beta = 0$ corresponds to a straight crack front. The results of the straight crack front obtained by numerically solving Dimarogonas' formula [20] are also presented in the figure for comparison with the current results. From Fig. 2, one can see that for $\beta = 0$ (straight front crack), the results of this paper agree well with that of Dimarogonas. As it was expected, and according to the literature results [18], the flexibility increases non-linearly with the crack depth. After considering the elliptical crack front, the flexibility is reduced. Especially for the circular front crack ($\beta = 1$), the reduction is the most obvious. This is explained as: With certain crack depth, the surface area of the curved front crack is smaller than that of the straight front crack. In addition, the SIFs along the curved crack front also change accordingly.

For the shaft rotating with a constant speed Ω, the elliptical surface crack is opened at its lower position and closed at its upper one due to gravity. Thus, the extra compliance would depend on its orientation with respect to direction of the gravitational force. The amount goes from zero ($0 \le \Omega t < \theta_A$, where θ_A represents $\angle AO_1D$ in Fig. 1) as the crack is closed to c'_η when it is half-opened, then to its maximum value c'_ξ when the crack is fully opened. This variance is periodic, and hence, a periodic time-varying system is expected. When the crack depth $\alpha_f = 0.5$, Fig. 3 shows the time-varying local flexibility $c'(t)$ in one full revolution with various crack shape factors ($\beta = 0, 0.4, 0.8, 1.0$). Obviously, increasing the shape factor would cause the amplitude of time-varying extra compliance reduce. Since only the values in $\xi - \eta$ directions are available, the curves in between are fitted by spline functions.

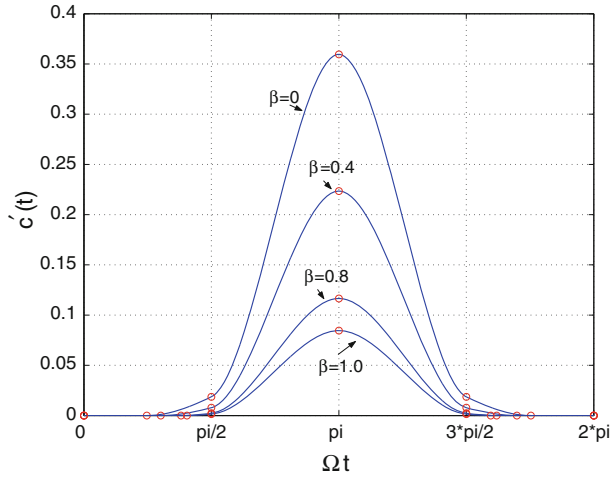

Fig. 3 The variation of crack flexibility with the shaft orientation for various β

3 Model of a rotating heavy shaft with elliptical front crack

A simply supported heavy shaft with an elliptical surface crack, as shown in Fig. 4, is modeled as an Euler–Bernoulli beam with constant angular rotating velocity Ω. The rotor span is l, and an elliptical crack locates at x^* on the shaft. The distributed load $p(x,t)$ equals to $\rho g A$ (ρ and A are the material density and cross-section area of the shaft) as the self-weight of the heavy shaft is the dominate external load. This is reasonable in most turbine rotors. Since the energy method is to be adopted for the equations of motion, the kinetic energy T, potential energy V_s of the shaft without crack and the work W done by the external load are expressed as follows

$$T = \frac{1}{2}\int_0^l \rho A\left[\frac{\partial y(x,t)}{\partial t}\right]^2 \mathrm{d}x, \quad V_s = \frac{1}{2}\int_0^l EI\left[\frac{\partial^2 y(x,t)}{\partial x^2}\right]^2 \mathrm{d}x, \quad W = \int_0^l \rho g A y(x,t)\mathrm{d}x \tag{12}$$

where $y(x,t)$ denotes the displacement function of the shaft in the vertical plane, and EI represents shaft bending rigidity. The released potential energy due to the elliptical surface crack could be obtained as

$$V_c = \frac{1}{2}c(t)\left[EI\frac{\partial^2 y(x^*,t)}{\partial x^2}\right]^2 \tag{13}$$

Thus, the total potential energy of the system is $V = V_s - V_c$.

The assumed modes method is now chosen for the equations of motion. Since the crack is theoretically of zero thickness, it is realized that the crack imposes significant effects on the local zone: e.g., stress intensity. As to the global behavior, it is believed that the natural modes of a cracked shaft are merely slightly perturbed from those of an uncracked shaft. It is hence reasonable to chose the natural modes of simply supported beam

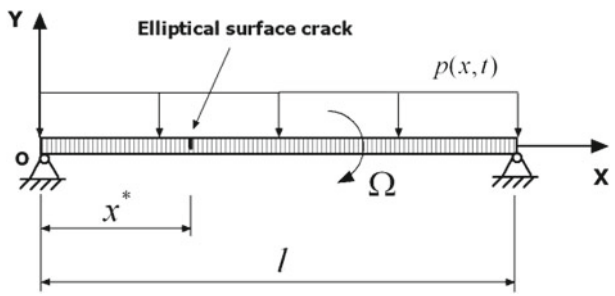

Fig. 4 A simply supported heavy rotating circular shaft with an elliptical surface crack

as a basis upon which to expand the displacement response of the cracked shaft. Then, both the kinetic and potential energies could be discretized with respect to the generalized coordinate. By employing Lagrange's equation, the discrete governing equations of motion in matrix form are obtained as

$$\mathbf{M}\ddot{\mathbf{q}}(t) + \mathbf{C}\dot{\mathbf{q}}(t) + \left[\mathbf{K}_0 - \mathbf{K}_c c'(t)\right]\mathbf{q}(t) = \mathbf{f}_g \tag{14}$$

where $\mathbf{q}$ is the vibration displacement vector, and the upper dot denotes differentiation with respect to time. The mass matrix of the shaft system is denoted by $\mathbf{M} = \mathrm{diag}[m_i]$. The $\mathbf{K}_0 = \mathrm{diag}[k_i]$ and $\mathbf{K}_c = [k_{ij}^c]$ are the constant and time-variable parts of the stiffness matrix for the system. If the proportional viscous damping is considered, then the damping matrix could be gained as $\mathbf{C} = \varsigma_1\mathbf{M} + \varsigma_2\mathbf{K}_0$, in which ς_1 and ς_2 are the mass and stiffness damping coefficients, respectively. $\mathbf{f}_g = [f_i]$ is the generalized force vector. The elements of the mass matrix, stiffness matrix and force vector could be, respectively, expressed as

$$m_i = \int_0^l \rho A \psi_i(x)\psi_i(x)\mathrm{d}x \tag{15}$$

$$k_i = \int_0^l E I \psi_i''(x)\psi_i''(x)\mathrm{d}x \tag{16}$$

$$k_{ij}^c = \frac{(1-\nu^2)EIR}{4}\psi_i''(x^*)\psi_j''(x^*) \tag{17}$$

$$f_i = \rho g A \int_0^l \psi_i(x)\mathrm{d}x \tag{18}$$

in which ψ_i and ψ_j are the ith and jth natural mode shape functions for the simply supported beam. The upper primes in ψ_i'' are differentiations with respect to x. Due to the existence of time-varying stiffness, the elliptical cracked rotating shaft is a typical parametrically excited system, as shown in Eq. (14). The parametric frequency and amplitude are related to the rotating angular speed and crack depth. Usually, the working speed of rotating machinery is lower than the third order of critical speed. Thus, the first three natural modes of the system are chosen in the following analysis, and the discrete system has three degrees of freedom.

4 Parametric instability and steady-state response analysis

4.1 Numerical determination of unstable boundaries

Determination of unstable boundaries is of the most interest in parametric instability analysis. Here, the Bolotin's method [21] is adopted to compute the boundaries of simple instability regions U_n^i. The starting points of U_n^i at the parametric frequency axis could be written as [22]

$$U_n^i \sim \frac{2}{n}\omega_i' \qquad (n = 1, 2, 3, \ldots) \tag{19}$$

in which ω_i' denotes the ith natural frequency of equivalent time-invariant system (the average equivalent frequency). For the boundaries of U_n^i $(n = 1, 3, 5, \ldots)$, the solution of actual parametric system should be expressed by $2T$ periodic solutions as

$$\mathbf{q}(t) = \sum_{k=1,3,5,\ldots}^{\infty}\left[\mathbf{a}_k \sin\left(\frac{k\Omega t}{2}\right) + \mathbf{b}_k \cos\left(\frac{k\Omega t}{2}\right)\right] \tag{20}$$

The time-periodic local flexibility $c'(t)$ is written in Fourier series form

$$c'(t) = c_0 + \sum_{j=1}^{\infty}\left[c_j \cos(j\Omega t) + d_j \sin(j\Omega t)\right] \tag{21}$$

Substituting Eqs. (20) and (21) into the homogenous form of Eq. (14) ($\mathbf{f}_g = 0$), one can obtain a series of equations with different orders of $\sin(\frac{k\Omega t}{2})$ and $\cos(\frac{k\Omega t}{2})$. Setting the coefficients of the equations with the same order to be zero, the homogenous equations satisfied by the $\mathbf{a}_k$ and $\mathbf{b}_k$ are obtained. The expressions, describing the parametric boundaries with unstable parameters, are gained by making the dominant equal to zero. If the U_1^i is concerned, the k in Eq. (20) is taken as 1 and the dominant for determining the unstable boundaries is computed as

$$\det\left(\begin{bmatrix} -\frac{1}{4}\Omega^2\mathbf{M} + \mathbf{K}_0 - c_0\mathbf{K}_c + \frac{1}{2}c_1\mathbf{K}_c & -\frac{1}{2}\Omega\mathbf{C} - \frac{1}{2}d_1\mathbf{K}_c \\ \frac{1}{2}\Omega\mathbf{C} - \frac{1}{2}d_1\mathbf{K}_c & -\frac{1}{4}\Omega^2\mathbf{M} + \mathbf{K}_0 - c_0\mathbf{K}_c - \frac{1}{2}c_1\mathbf{K}_c \end{bmatrix}\right) = 0 \tag{22}$$

If more instability regions (U_3^i, U_5^i and so on) are taken into account, the number of values for the k in Eq. (20) should be increased correspondingly.

For the boundaries of U_n^i ($n = 2, 4, 6, \ldots$), the solution of actual parametric system should be expressed by T periodic solutions as

$$\mathbf{q}(t) = \mathbf{b}_0 + \sum_{k=2,4,6,\ldots}^{\infty} \left[\mathbf{a}_k \sin\left(\frac{k\Omega t}{2}\right) + \mathbf{b}_k \cos\left(\frac{k\Omega t}{2}\right)\right] \tag{23}$$

Substituting Eq. (23) into (14), the boundaries of the other half of simple instability regions, such as the U_2^i, U_4^i and U_6^i, are obtained through a similar solution process with that of the $2T$ periodic solution. If only the U_2^i is interest, the gained dominant is expressed as

$$\det\left(\begin{bmatrix} \mathbf{K}_0 - c_0\mathbf{K}_c & -\frac{1}{2}d_1\mathbf{K}_c & -\frac{1}{2}c_1\mathbf{K}_c \\ -d_1\mathbf{K}_c & -\Omega^2\mathbf{M} + \mathbf{K}_0 - c_0\mathbf{K}_c + \frac{1}{2}c_2\mathbf{K}_c & -\Omega\mathbf{C} - \frac{1}{2}d_2\mathbf{K}_c \\ -c_1\mathbf{K}_c & \Omega\mathbf{C} - \frac{1}{2}d_2\mathbf{K}_c & -\Omega^2\mathbf{M} + \mathbf{K}_0 - c_0\mathbf{K}_c - \frac{1}{2}c_2\mathbf{K}_c \end{bmatrix}\right) = 0 \tag{24}$$

More simple instability boundaries could be gained by adding the number of values of the parameter k in Eq. (23).

4.2 Steady-state forced response analysis

The steady-state forced response of the cracked shaft under self-weight excitation is mainly considered in the paper. The harmonic balance method is utilized to compute the amplitude values of forced response spectra. By taking $\mathbf{y}(t) = [\dot{\mathbf{q}}(t) \quad \mathbf{q}(t)]^T$, Eq. (14) could be rewritten in state space form as

$$\dot{\mathbf{y}}(t) = \mathbf{A}(t)\mathbf{y}(t) + \mathbf{f}_s \tag{25}$$

in which the time-periodic coefficient matrix $\mathbf{A}(t)$ and force vector $\mathbf{f}_s$ are expressed as

$$\mathbf{A}(t) = -\begin{bmatrix} \mathbf{0} & \mathbf{M} \\ \mathbf{M} & \mathbf{C} \end{bmatrix}^{-1} \begin{bmatrix} -\mathbf{M} & \mathbf{0} \\ \mathbf{0} & \mathbf{K}_0 - \mathbf{K}_c c'(t) \end{bmatrix} \tag{26}$$

$$\mathbf{f}_s = \begin{bmatrix} \mathbf{0} & \mathbf{M} \\ \mathbf{M} & \mathbf{C} \end{bmatrix}^{-1} \begin{bmatrix} \mathbf{0} \\ \mathbf{f}_g \end{bmatrix} \tag{27}$$

The steady-state forced response of the elliptical cracked shaft could be represented as

$$\mathbf{y}(t) = \sum_{s=-\infty}^{\infty} \mathbf{y}_s e^{is\Omega t} \tag{28}$$

where $i = \sqrt{-1}$. The periodic coefficient matrix $\mathbf{A}(t)$ could also be rewritten by Fourier series

$$\mathbf{A}(t) = \sum_{k=-\infty}^{\infty} \mathbf{A}_k e^{ik\Omega t} \tag{29}$$

Substituting Eqs. (28) and (29) into (25) and simplifying by setting the same harmonic coefficients zero, then one can obtain the following infinite-dimensional linear algebraic equations about the steady-state response spectral amplitudes

$$\begin{bmatrix} \vdots & \vdots & \vdots & \vdots & \vdots & \vdots & \vdots & \vdots & \vdots & \vdots & \vdots \\ \cdots & \boldsymbol{\Xi}_4 & \mathbf{A}_{-1} & \mathbf{A}_{-2} & \mathbf{A}_{-3} & \mathbf{A}_{-4} & \mathbf{A}_{-5} & \mathbf{A}_{-6} & \mathbf{A}_{-7} & \mathbf{A}_{-8} & \cdots \\ \cdots & \mathbf{A}_1 & \boldsymbol{\Xi}_3 & \mathbf{A}_{-1} & \mathbf{A}_{-2} & \mathbf{A}_{-3} & \mathbf{A}_{-4} & \mathbf{A}_{-5} & \mathbf{A}_{-6} & \mathbf{A}_{-7} & \cdots \\ \cdots & \mathbf{A}_2 & \mathbf{A}_1 & \boldsymbol{\Xi}_2 & \mathbf{A}_{-1} & \mathbf{A}_{-2} & \mathbf{A}_{-3} & \mathbf{A}_{-4} & \mathbf{A}_{-5} & \mathbf{A}_{-6} & \cdots \\ \cdots & \mathbf{A}_3 & \mathbf{A}_2 & \mathbf{A}_1 & \boldsymbol{\Xi}_1 & \mathbf{A}_{-1} & \mathbf{A}_{-2} & \mathbf{A}_{-3} & \mathbf{A}_{-4} & \mathbf{A}_{-5} & \cdots \\ \cdots & \mathbf{A}_4 & \mathbf{A}_3 & \mathbf{A}_2 & \mathbf{A}_1 & \boldsymbol{\Xi}_0 & \mathbf{A}_{-1} & \mathbf{A}_{-2} & \mathbf{A}_{-3} & \mathbf{A}_{-4} & \cdots \\ \cdots & \mathbf{A}_5 & \mathbf{A}_4 & \mathbf{A}_3 & \mathbf{A}_2 & \mathbf{A}_1 & \boldsymbol{\Xi}_{-1} & \mathbf{A}_{-1} & \mathbf{A}_{-2} & \mathbf{A}_{-3} & \cdots \\ \cdots & \mathbf{A}_6 & \mathbf{A}_5 & \mathbf{A}_4 & \mathbf{A}_3 & \mathbf{A}_2 & \mathbf{A}_1 & \boldsymbol{\Xi}_{-2} & \mathbf{A}_{-1} & \mathbf{A}_{-2} & \cdots \\ \cdots & \mathbf{A}_7 & \mathbf{A}_6 & \mathbf{A}_5 & \mathbf{A}_4 & \mathbf{A}_3 & \mathbf{A}_2 & \mathbf{A}_1 & \boldsymbol{\Xi}_{-3} & \mathbf{A}_{-1} & \cdots \\ \cdots & \mathbf{A}_8 & \mathbf{A}_7 & \mathbf{A}_6 & \mathbf{A}_5 & \mathbf{A}_4 & \mathbf{A}_3 & \mathbf{A}_2 & \mathbf{A}_1 & \boldsymbol{\Xi}_{-4} & \cdots \\ \vdots & \vdots & \vdots & \vdots & \vdots & \vdots & \vdots & \vdots & \vdots & \vdots & \vdots \end{bmatrix} \begin{bmatrix} \vdots \\ \mathbf{y}_{-4} \\ \mathbf{y}_{-3} \\ \mathbf{y}_{-2} \\ \mathbf{y}_{-1} \\ \mathbf{y}_0 \\ \mathbf{y}_1 \\ \mathbf{y}_2 \\ \mathbf{y}_3 \\ \mathbf{y}_4 \\ \vdots \end{bmatrix} = \begin{bmatrix} \vdots \\ \mathbf{0} \\ \mathbf{0} \\ \mathbf{0} \\ \mathbf{0} \\ \mathbf{f}_s \\ \mathbf{0} \\ \mathbf{0} \\ \mathbf{0} \\ \mathbf{0} \\ \vdots \end{bmatrix} \tag{30}$$

where $\boldsymbol{\Xi}_s = \mathbf{A}_0 + is\Omega\mathbf{I}$ ($s = \cdots, -2, -1, 0, 1, 2, \ldots$), and $\mathbf{I}$ is the unit matrix. As indicated in the literature, such equations can be truncated to a finite-dimensional ones in order to obtain an approximate numerical solution for the steady-state response spectral amplitudes. The first four response spectra will be taken into account to meet the accuracy requirements.

5 Computation and discussions

A practical used heavy shaft [6] is taken as a numerical example for computation and discussions. The shaft parameters are as follows: $l = 10\,\text{m}$, $R = 0.5\,\text{m}$, $\rho = 7,850\,\text{kg/m}^3$, $E = 2.1 \times 10^{11}\,\text{Pa}$, $\nu = 0.3$. A dimensionless parameter $\chi^* = x^*/l$ is defined to describe the relative position of the elliptical crack on the shaft.

5.1 Parametric instability regions

Without the elliptical crack, the first three natural frequencies of the shaft are as follows: $\omega_1' = 127.6\,\text{rad/s}$, $\omega_2' = 510.5\,\text{rad/s}$ and $\omega_3' = 1,148.6\,\text{rad/s}$. From Eq. (19), the starting points of simple instability regions are as follows: $U_1^1 \approx 255.2\,\text{rad/s}$, $U_1^2 \approx 1,021\,\text{rad/s}$ and so on. In actual, due to damping, the high orders of instability regions (usually $n > 2$ in Eq. (19)) would be greatly weakened. The above two instability regions are mainly considered in the following analysis.

The boundaries of U_1^1 and U_1^2 in the parameter's plane (rotating speed Ω versus crack depth α_f) are solved using Eq. (22). The discrete state transition matrix (DSTM) method is another classical method for the parametric stability analysis. Utilizing the DSTM method, the instable regions are also determined in order to verify the results gained in this paper. Here, a numerical methodology presented by Friedmann [23] is utilized to estimate the DSTM. The comparisons of U_1^1 and U_1^2 for $\beta = 0.0$ and $\chi^* = 0.3$ are given in Fig. 5. Obviously, the two aspects of results agree well with each other, indicating that the parametric instability analysis is reasonable and believable.

The effects of shape factor β, crack position χ^* and damping ($\varsigma_1 = 1.0$ and $\varsigma_2 = 2.3\text{e}-7$) upon the instability regions are investigated and shown in Figs. 6, 7 and 8, respectively. It is shown from the figures that the starting points of U_1^1 and U_1^2 on the rotating speed axis are just about 255.2 and 1,021 rad/s. With the increasing in α_f, the two instability regions become wide and shift toward the lower rotating speed ranges. This is because the parametric excitation due to crack is enhanced as the crack grows. Moreover, the average natural frequency of the cracked shaft is also reduced, and thus, the instability regions would appear in lower rotating speed ranges.

From Fig. 6, one can see that the instability regions become smaller and shift to the right with the increasing in β. For given crack depth, according to the discussions in Sect. 2, the local flexible coefficients are reduced if the β is increased. Thus, the parametric excitation amplitude is depressed, and the instability regions become small.

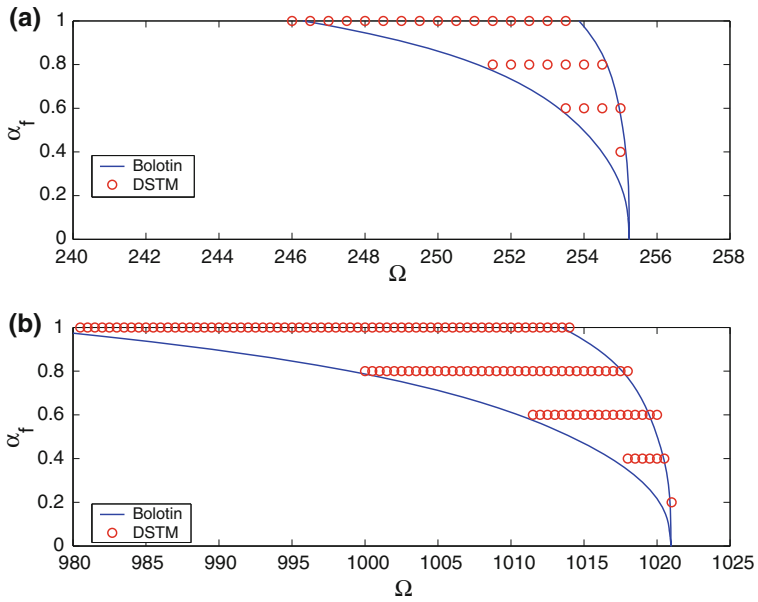

Fig. 5 Comparisons of unstable boundaries obtained by the Bolotin's method and the DSTM method for $\beta = 0.0$ and $\chi^* = 0.3$: **a** U_1^1; **b** U_1^2

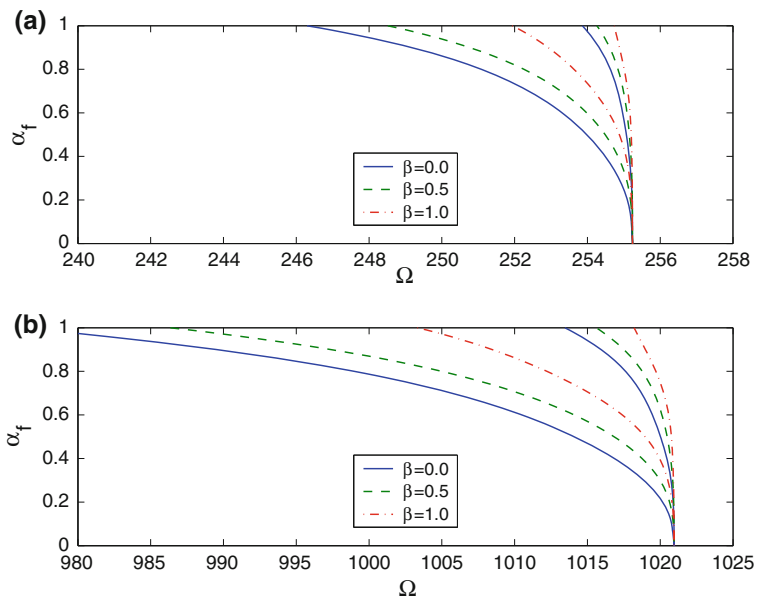

Fig. 6 The effect of β upon the two instability regions for $\chi^* = 0.3$: **a** U_1^1; **b** U_1^2

When the crack position is approaching the midpoint of the shaft ($\chi^* = 0.45$), the U_1^1 has greater ranges compared with the cases of $\chi^* = 0.25$ and $\chi^* = 0.35$, as shown in Fig. 7a. However, one can find from Fig. 7b that the range of U_1^2 with $\chi^* = 0.25$ is wider than that of $\chi^* = 0.35$ and $\chi^* = 0.45$. This could be explained in the context of nodal location. The U_1^1 is related to the first natural mode of the simply supported shaft. When $\chi^* = 0.45$, the elliptical crack position is just the position having greater modal deformation. In this case, the crack would have the bigger influence on the U_1^1. With the crack location moving toward the supported points ($\chi^* = 0.35$ or $\chi^* = 0.25$), the crack influence is depressed. In case of U_1^2, the modal deformation of $\chi^* = 0.25$ at the second mode shape of the simply supported shaft is larger than that of $\chi^* = 0.35$ or 0.45. Thus, the U_1^2 with $\chi^* = 0.25$ has wider range than the other cases. From Fig. 8, one can find that the U_1^1 and

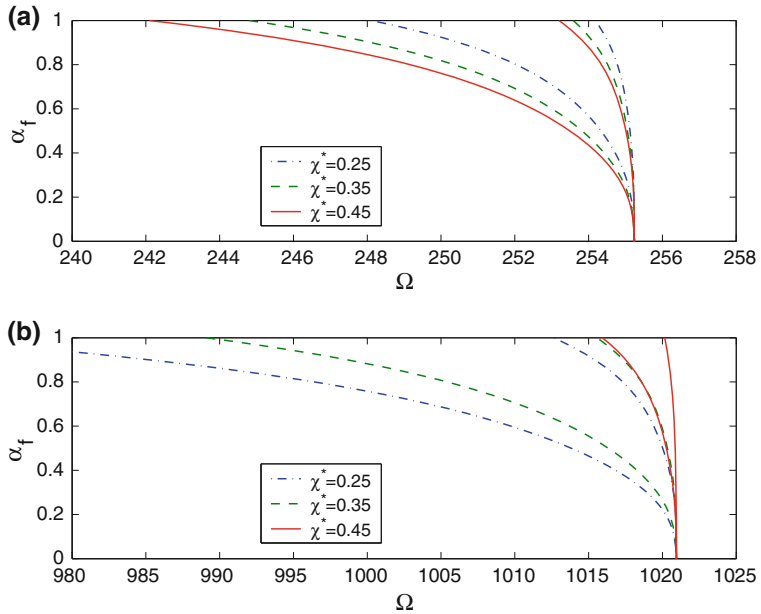

Fig. 7 The effect of χ^* upon the two instability regions for $\beta = 0.1$: **a** U_1^1; **b** U_1^2

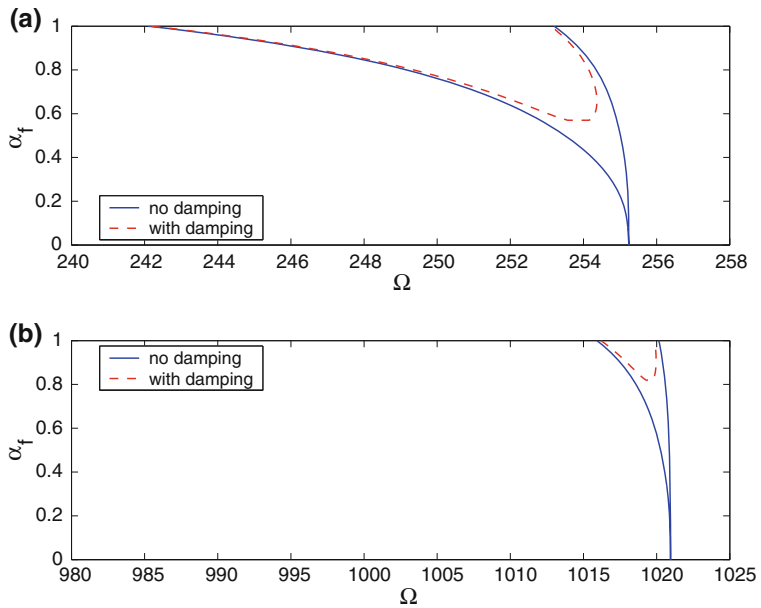

Fig. 8 The effect of damping upon the two instability regions for $\beta = 0.1$ and $\chi^* = 0.45$: **a** U_1^1; **b** U_1^2

U_1^2 are attenuated by the damping, especially for the shallow surface cracks. It is indicated that the parametric instability induced by small surface crack is not obvious in actual practice.

5.2 Steady-state response of cracked shaft under both parametric and self-weight excitations

For small surface cracks, the damped shaft system remains stable in most rotating speed ranges. In this case, the steady-state response of the system subjected to parametric and self-weight excitations would be of most interest. The first four response spectral amplitudes are solved utilizing the harmonic balance method in Sect. 4.2. Then, the periodically forced response vector $\mathbf{y}(t)$ is approximately obtained through Eq. (28). Here, the results

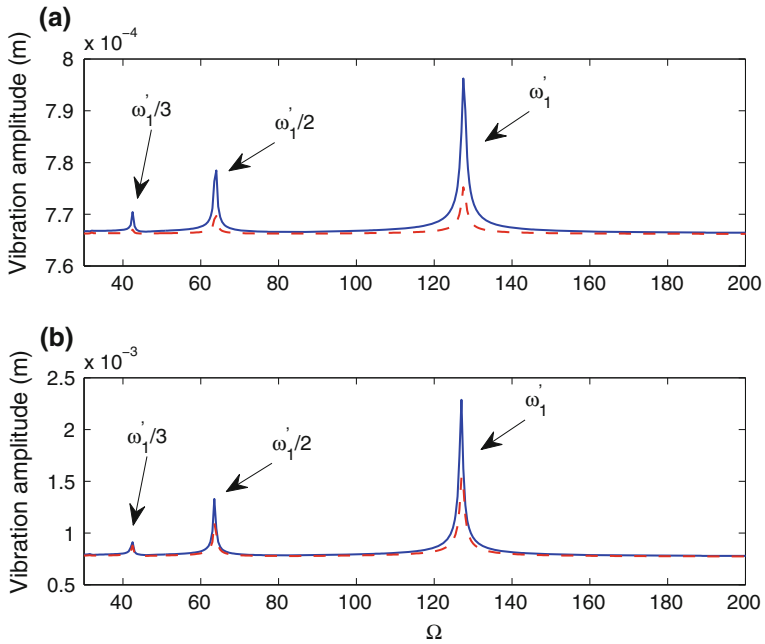

Fig. 9 Variations of the maximum vibration amplitude with rotating speed Ω in [30,200] for $\chi^* = 0.5$: **a** $\alpha_f = 0.1$; **b** $\alpha_f = 0.5$. *Solid lines* $\beta = 0.0$; *dashed lines* $\beta = 0.5$

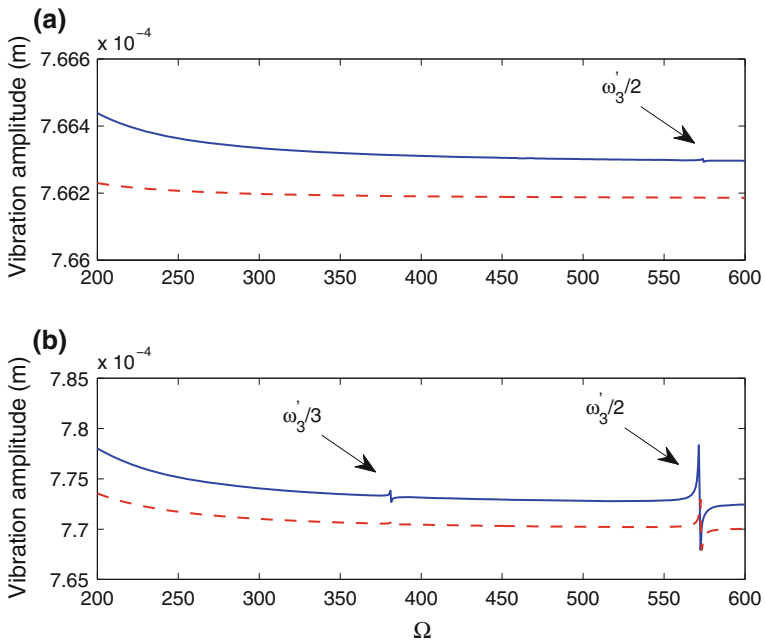

Fig. 10 Variations of the maximum vibration amplitude with rotating speed Ω in [200,600] for $\chi^* = 0.5$: **a** $\alpha_f = 0.1$; **b** $\alpha_f = 0.5$. *Solid lines* $\beta = 0.0$; *dashed lines* $\beta = 0.5$

for the maximum displacement response amplitude of the first degree of freedom of the discrete shaft system are given in Figs. 9, 10, 11, 12, with various elliptical crack parameters (crack depth, shaft factor and crack position). The damping coefficients are set to be $\varsigma_1 = 1.0$ and $\varsigma_2 = 2.3\text{e} - 7$. In order to show the response amplitude curves clearly, two rotating speed ranges around the two uncracked shaft natural frequencies (Ω in [30,200] and [200,600]) are, respectively, plotted in the figures.

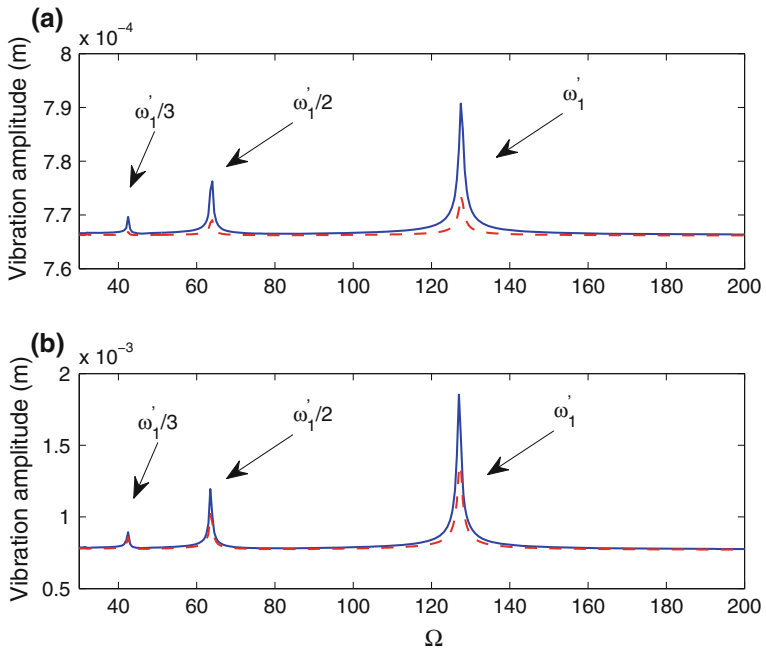

Fig. 11 Variations of the maximum vibration amplitude with rotating speed Ω in [30,200] for $\chi^* = 0.35$: **a** $\alpha_f = 0.1$; **b** $\alpha_f = 0.5$. *Solid lines* $\beta = 0.0$; *dashed lines* $\beta = 0.5$

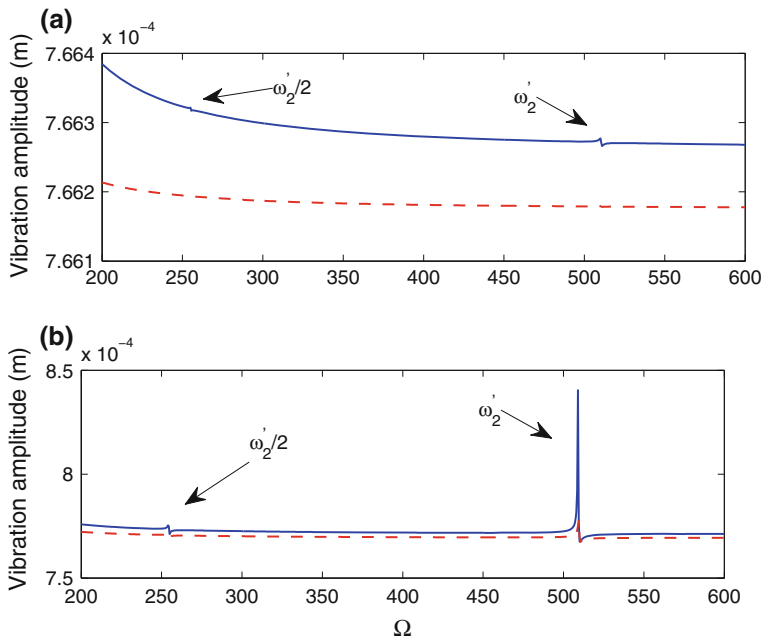

Fig. 12 Variations of the maximum vibration amplitude with rotating speed Ω in [200,600] for $\chi^* = 0.35$: **a** $\alpha_f = 0.1$; **b** $\alpha_f = 0.5$. *Solid lines* $\beta = 0.0$; *dashed lines* $\beta = 0.5$

It is shown from Figs. 9, 10, 11, 12 that there are many peaks in the two rotating speed ranges. This phenomenon is referred to as the subharmonic resonance and occurs when the rotational speed is an integer fraction of the system frequency, i.e., $\Omega = \omega_i'/n\ (n = 1, 2, 3, \ldots)$. These resonances are identified and marked in the figures. Similar phenomena have been observed in many investigations [6,24,25]. Moreover, the vibration amplitude in the non-resonant range is 7.66×10^{-4}m, which approximately equals to the static deformation

of the shaft under self-gravity. Thus, one can see that the steady-state response analysis is reasonable and believable.

Every resonant peaks of deeper cracks are all higher than those of lower cracks, indicating that the resonances become more and more severe as the crack grows. For certain crack depth, increasing the shape factor would reduce the resonant amplitudes. This is because the parametric excitation induced by curved surface crack has lower amplitude, and thus, the subharmonic resonances become weakened. Compared with Figs. 9, 10, and 11, 12, one can see that the crack position also has impact on the subharmonic resonances. For $\chi^* = 0.5$, the crack is just at the nodal line of the second modal shape of the simply supported shaft. Thus, the resonances related to the second natural mode do not appear. Instead, the resonances related to the third natural mode, such as $\omega_3'/2$ and $\omega_3'/3$, are found in Fig. 10. When $\chi^* = 0.35$, as shown in Fig. 12, the second subharmonic resonances ($\omega_2'/2$ and $\omega_2'/3$) appear as the crack is away from the nodal line of the modal shape. In this case, the crack position is near the nodal line of third mode shape. Thus, the third-order resonant peaks are not obvious due to the attenuation effect of damping. When the crack is approaching the shaft support point, the resonances related to the first natural mode (ω_1', $\omega_1'/2$ and $\omega_1'/3$) are reducing, which could be found by comparing the peak amplitudes in Figs. 9 and 11.

6 Conclusions

The dynamic instability and steady-state response of a rotating heavy shaft containing an elliptical surface crack are studied using the Bolotin's method and harmonic balance method. The effects of crack parameters and damping are considered and discussed in the dynamic analysis. Some conclusions are summarized as follows: Both the ranges of instability regions and steady-state response amplitudes all become smaller and lower with the increasing in crack shape factor. For deeper surface crack, the instability regions are wider and tend to appear in lower rotating speed range. In this case, the subharmonic resonances seem to be more intensive and severe. The influence of crack position on the dynamic behavior of crack shaft should be discussed in the context of nodal location. If the crack locates at certain position with greater modal deformation (such as the midpoint for the first natural mode), then it would have more significant impact on the instability regions and dynamic responses, which are related to this order of natural mode. However, its impact would reduce and even disappear as it approaches the nodal line of the mode shape. The instability regions would be attenuated as long as the damping is taken into account, especially for the shallow surface cracks.

Acknowledgments The research work described in the paper was supported by the National Science Foundation of China under Grant no. 10732060/51075224 and the China Postdoctoral Science Foundation under Grant no. 20100480012.

References

1. Wauer, J.: Dynamics of cracked rotors: a literature survey. Appl. Mech. Rev. **43**, 13–17 (1990)
2. Gasch, R.A.: A survey of the dynamic behavior of simple rotating shaft with a transverse crack. J. Sound Vib. **160**, 313–332 (1993)
3. Dimarogonas, A.D.: Vibration of cracked structures: a state of the art review. Eng. Frac. Mech. **55**(5), 831–875 (1996)
4. Papadopoulos, C.A.: The strain energy release approach for modeling cracks in rotors: A state of the art review. Mech. Syst. Signal Process. **22**, 763–789 (2008)
5. Bachschmid, N., Pennacchi, P., Tanzi, E.: Cracked rotors: a survey on static and dynamic behaviour including modelling and diagnosis. Springer, Berlin, Heidelberg (2010)
6. Huang, S.C., Huang, Y.M., Shieh, S.M.: Vibration and stability of a rotating shaft containing a transverse crack. J. Sound Vib. **162**(3), 387–401 (1993)
7. Zou, J., Chen, J., Niu, J.C. et al.: Discussion on the local flexibility due to the crack in a cracked rotor system. J. Sound Vib. **262**, 365–369 (2003)
8. Chasalevris, A.C., Papadopoulos, C.A.: Identification of multiple cracks in beams under bending. Mech. Syst. Signal Process. **20**, 1631–1673 (2006)
9. Yang, F.P., Kuang, Z.B., Shlyannikov, V.N.: Fatigue crack growth for straight-fronted edge crack in a round bar. Int. J. Fatigue **28**, 431–437 (2006)
10. Bachschmid, N., Pennacchi, P., Tanzi, E.: On the evolution of vibrations in cracked rotors. The 8th IFToMM International Conference on Rotor Dynamics, September 12–15. KIST, Seoul, South Korea (2010)
11. Athanassiadis, A., Boissenot, J.M., Brevet, P. et al.: Linear elastic fracture mechanics computations of cracked cylindrical tensioned bodies. Int. J. Fract. **17**(6), 553–566 (1981)
12. Murakami, Y., Tsuru, H.: Stress-Intensity Factor Equations for Semi-Elliptical Surface Crack in Shaft Under Bending. Stress Intensity Factors Handbook. pp. 657–658. Pergamon Press, Oxford (1987)

13. Carpinteri, A., Brighenti, R., Spagnoli, A.: Surface flaws in cylindrical shafts under rotary bending. Fatigue Fract. Eng. Mater. Struct. **21**, 1027–1035 (1998)
14. Shih, Y.S., Chen, J.J.: Analysis of fatigue crack growth on a cracked shaft. Int. J. Fatigue **19**, 477–485 (1997)
15. Shih, Y.S., Chen, J.J.: The stress intensity factor study of an elliptical cracked shaft. Nucl. Eng. Des. **214**, 137–145 (2002)
16. Fonte, M., Freitas, M.: Stress intensity factors for semi-elliptical surface cracks in round bars under bending and torsion. Int. J. Fatigue **21**, 457–463 (1999)
17. Shin, C.S., Cai, C.Q.: Experimental and finite element analyses on stress intensity factors of an elliptical surface crack in a circular shaft under tension and bending. Int. J. Fract. **129**, 239–264 (2004)
18. Rubio, L., Munoz-Abella, B.: Flexibility coefficients of a shaft with an elliptical front crack. In: Institution of Mechanical Engineers—9th International Conference on Vibrations in Rotating Machinery, pp. 657–667. Exeter, UK (2008)
19. Rubio, L., Munoz-Abella, B., Loaiza, G.: Static behaviour of a shaft with an elliptical crack. Mech. Syst. Signal Process. **25**, 1674–1686 (2011)
20. Dimarogonas, A.D., Paipetis, S.A.: Analytical Methods in Rotor Dynamics. Applied Science Publishers, London and New York (1983)
21. Bolotin, V.V.: Dynamic Stability of Elastic Systems. Holden-Day, San Francisco (1964)
22. Nayfeh, A.H., Mook, D.T.: Nonlinear Oscillations. Wiley, New York (1979)
23. Friedmann, P., Hammond, E., Woo, T.H.: Efficient numerical treatment of periodic systems with application to stability problems. Int. J. Numer. Methods Eng. **11**, 1117–1136 (1977)
24. Grabowski, B.: The vibrational behavior of a turbine rotor containing a transverse crack. Trans. ASME J. Mech. Des. **102**, 123–128 (1980)
25. Mayes, I.W., Davies, W.G.R.: Analysis of the response of a multi-rotor bearing system containing a transverse crack in a rotor. Tran. ASME J. Vib. Acoust. Stress Reliab. Des. **106**(1), 139–145 (1984)